REPORT No. 878

ANALYSIS OF PERFORMANCE OF JET ENGINE FROM CHARACTERISTICS OF COMPONENTS I——AERODYNAMIC AND MATCHING CHARACTERISTICS OF TURBINE COMPONENT DETERMINED WITH COLD AIR

By Arthur W. Goldstein

SUMMARY

The performance of the turbine component of an NACA research jet engine was investigated with cold air. The interaction and the matching of the turbine with the NACA eight-stage compressor were computed with the combination considered as a jet engine. The over-all performance of the engine was then determined. The internal aerodynamics were studied to the extent of investigating the performance of the first stator ring and its influence on the turbine performance. For this ring, the stream-filament method for computing velocity distribution permitted efficient sections to be designed, but the design condition of free-vortex flow with uniform axial velocities was not obtained. The actual air flow was 0.964 of the design value at design pressure ratio and speed and was 0.98 at design speed and enthalpy drop. Rotative speed for optimum efficiency (0.875) was 180 revolutions per second as compared with the design speed of 134 revolutions per second (efficiency, 0.823).

INTRODUCTION

The NACA two-stage turbine was designed and built under the direction of Eastman N. Jacobs by the NACA Cleveland laboratory staff as a component of a jet engine, which served as a tool for the study of the behavior of this engine type. The compressor component of the engine was to be the NACA eight-stage compressor discussed in references 1 to 3. A turbine investigation was made at the Cleveland laboratory during 1945 with an inlet-air temperature of 190° F and a range of equivalent turbine speeds from 102 to 182 revolutions per second and pressure ratios from 1.16 to 2.60. This investigation was conducted to evaluate the blade-design procedure by determining the performance of the first stator ring and its influence on over-all turbine performance, to determine the performance of the turbine without the constraint imposed by operating the compressor and the turbine together, and to use these data to investigate the matching of the turbine and the compressor.

DESCRIPTION OF THE TURBINE

Design conditions.—The turbine was designed for the following operating conditions: inlet pressure, 2400 pounds per square foot; inlet-gas temperature, 1400° R; gas flow, 4.18 pounds per second; power output to the shaft, 296.5 horsepower; and rotor speed, 13,010 rpm. For operation in the jet engine, the assumed compressor pressure ratio was 3.36; the compressor inlet-air temperature, 440° R; and the compressor inlet-air pressure, 739 pounds per square foot. Flight speed was 470 miles per hour and altitude, 33,000 feet.

The turbine work output was so divided between the stages that the ratio of the temperature drop to average temperature for each stage was the same for both stages in order to maintain Mach numbers approximately the same for the two stages. The velocities between blade rings are shown in the following table:

Station	Axial velocity (ft/sec)	Tangential velocity at root (ft/sec)	Tangential velocity at tip (ft/sec)
Entrance stator I	209	0	0
Exit stator I	228	933	600
Entrance rotor I	228	422	−195
Exit rotor I	269	−828	−999
Entrance stator II	269	−317	−204
Exit stator II	290	898	578
Entrance rotor II	290	337	−217
Exit rotor II	346	−816	−991
Entrance stator III	346	−305	−196

These velocities were computed on the assumption of radial equilibrium, constant gas energy and entropy, and free-vortex flow from root to tip. These assumptions result in a constant axial velocity over the blade span, which may be demonstrated by consideration of the condition for radial equilibrium of pressure with no radial flow:

$$dp=\rho\frac{c_u^2}{r}r \tag{1}$$

where

p pressure, (lb/sq ft)
ρ density, (slug/cu ft)
c_u whirl-velocity component, (ft/sec)
r distance from axis of annular channel, (ft)

For convenience, all symbols used in this report are defined in appendix A.

The equation relating enthalpy change to entropy change is

$$dH=TdS+\frac{dp}{\rho}$$

where

H enthalpy, (ft-lb/slug)
T gas temperature, (° R)
S gas entropy, (ft-lb/(slug)(° R))

Therefore,

$$\frac{dp}{\rho}=dH-TdS=\frac{c_u^2}{r}dr$$

The energy equation is

$$dH_T=dH+d\left(\frac{c^2}{2}\right)$$

where c is the velocity in feet per second and the subscript T indicates stagnation state. Insertion into the equilibrium equation gives

$$dH_T-d\left(\frac{c^2}{2}\right)-TdS=\frac{c_u^2}{r}dr \tag{2}$$

If the flow is isentropic and the gas of uniform energy level,

$$dH_T=dS=0$$

and

$$d\left(\frac{c_a^2+c_u^2}{2}\right)=d\left(\frac{c^2}{2}\right)=-\frac{c_u^2}{r}dr \tag{3}$$

where c_a is the axial-velocity component in feet per second. Other useful forms of equation (3) are

$$0=d\left(\frac{c_a^2}{2}\right)+c_u dc_u+c_u^2\frac{dr}{r}=d\left(\frac{c_a^2}{2}\right)+\frac{1}{2r^2}d(rc_u)^2 \tag{4}$$

If the moment of momentum is constant, $d(rc_u)=0$ and c_a is therefore constant. The type of motion where rc_u is a constant is designated free-vortex flow because the radial distribution of whirl velocity is the same as that for an isolated vortex filament.

In the design procedure, the assumption was made that all the losses took place in the rotor and the stage efficiency was 0.90 based on total pressures and temperatures.

The flow channels between the blades were designed to provide guidance at the exit by making both walls nearly parallel to the desired flow angle for a distance approximately equal to the exit-channel width. From the channel exit toward the entrance, along the suction (convex) side of the blade, the radius of curvature was decreased as the channel width increased toward the region near the leading edge. The camber line was pointed in the direction of the incoming flow. Blade trailing edges were 0.03 inch thick, except for the second row of stator blades, which were castings with trailing-edge thicknesses varying from 0.020 to 0.015 inch. The leading-edge radius of curvature was taken as 15 percent of the maximum thickness.

When a blade section had thus been roughly designed, the velocity distribution on the suction side of the blade was computed by means of the stream-filament theory described in reference 4. This method was modified to account for the varying mass flow per unit blade height in the channel due to radial flow by assuming for each section a linear variation of the mass flow per unit blade height along the middle streamline from the entrance to the exit values. If necessary, the suction-surface shape was modified to keep the velocity on this surface nearly constant. No information was obtained in this fashion about the airfoil nose or the projecting suction side of the blade (section A–B, fig. 1) because the stream-filament theory of flow in channels is inapplicable in this region. Figure 1 shows the root section of the first stator ring.

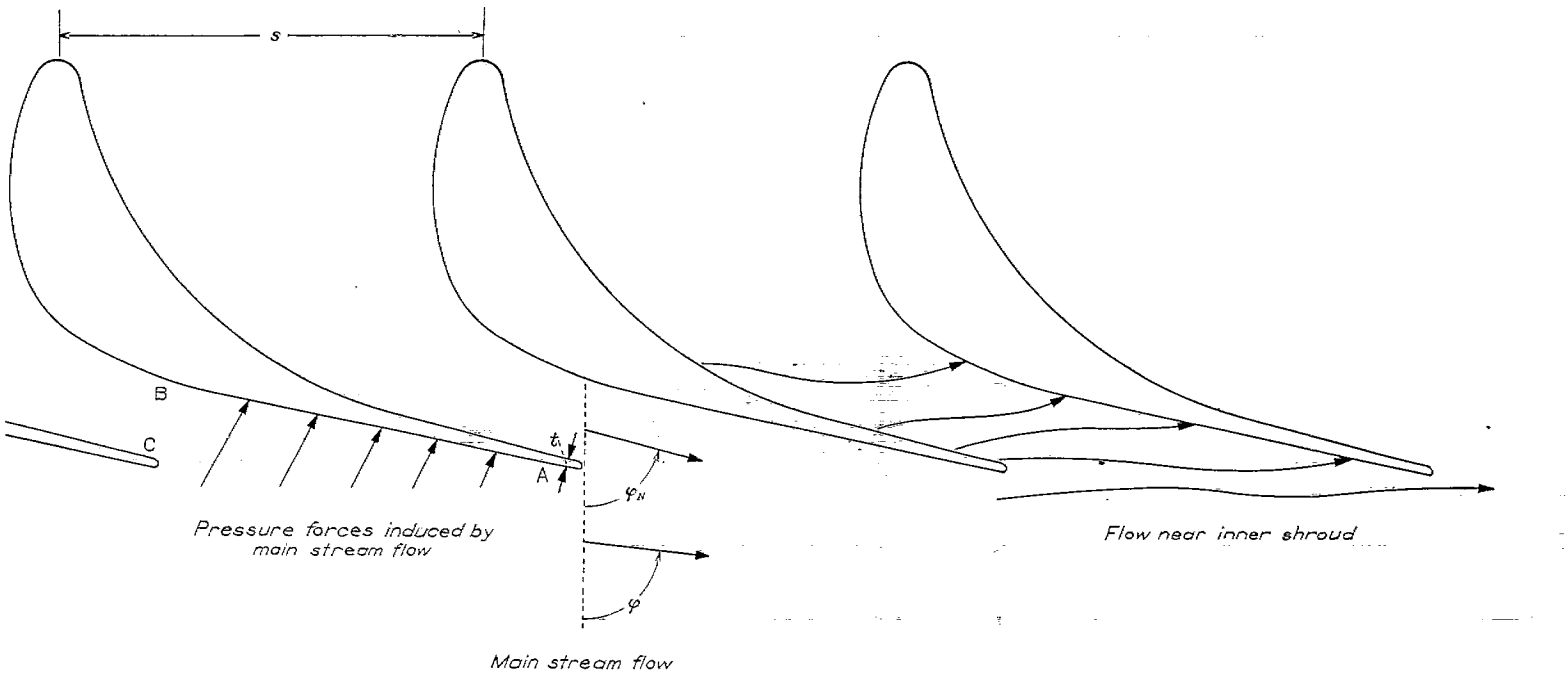

FIGURE 1.—Cascade notation and flow characteristics of root section of first stator ring of NACA two two-stage turbine

Construction.—The turbine consists of two stages of rotor blades and three stages of stator blades. Reaction in both the rotor stages may be increased by the use of a final stator stage, which also insures efficient jet-nozzle operation over a wide range of turbine and compressor operating conditions by eliminating the rotation of the discharged gas. A downstream view of the first ring of stator blades is shown in figure 2. The second ring (upstream view) and third ring of stators (downstream view) are shown in figures 3 and 4, respectively. The rotor is shown in figure 5. All rotor and stator blades had an inner diameter of 9 inches and an outer diameter of 14 inches. All blades had a radial tip clearance of 0.035 inch. The rotor blades are fastened to the wheel by a fir-tree-type blade base. For this investigation, a set of sleeve bearings was used.

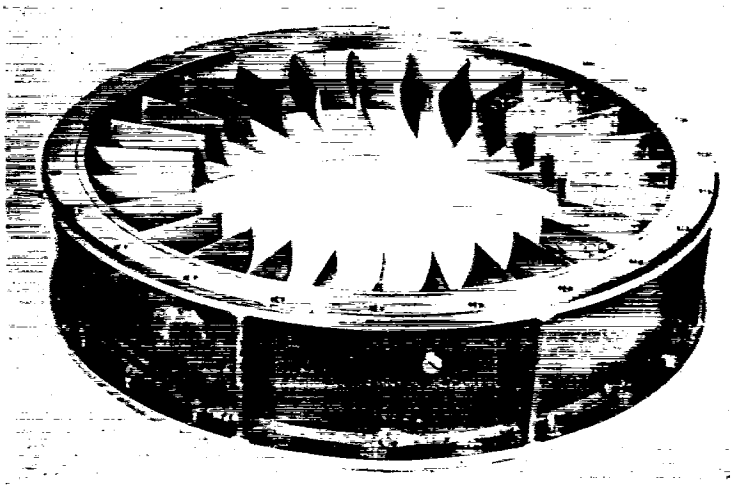

FIGURE 1.—Third stator ring of NACA two-stage turbine. Downstream view

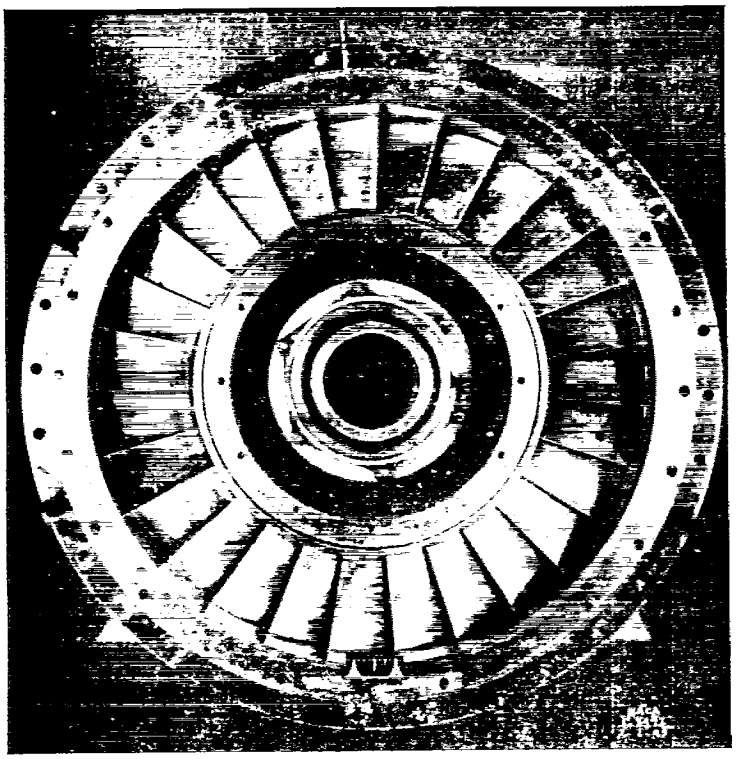

FIGURE 2.—First stator ring of NACA two-stage turbine. Downstream view.

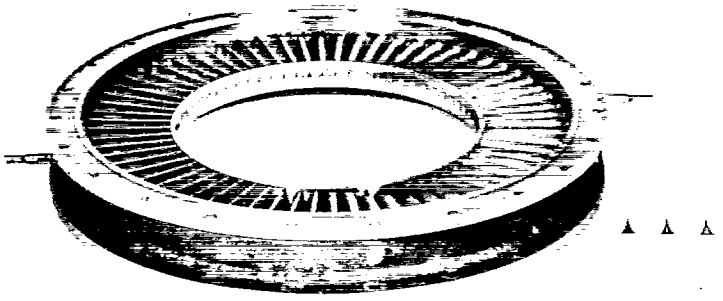

FIGURE 3.—Second stator ring of NACA two-stage turbine. Upstream view

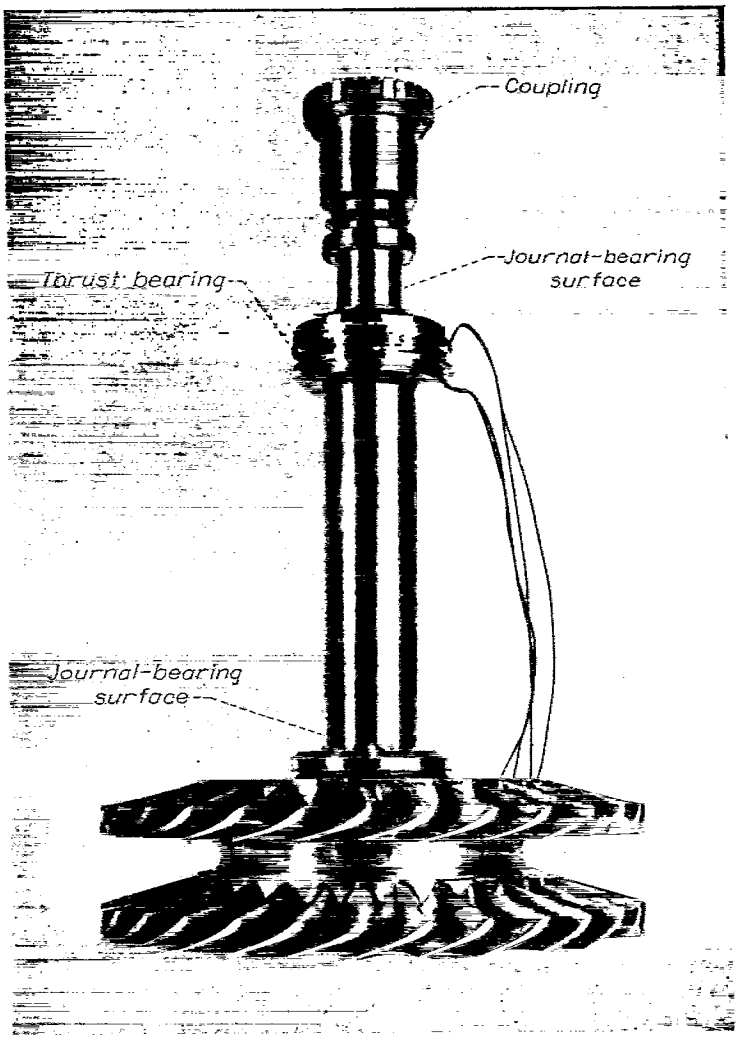

FIGURE 5.—Rotor of NACA two-stage turbine.

APPARATUS

Apparatus for investigation of cascade ring.—The first stator ring was mounted between two concentric pipes with a bellmouth entrance and room air was drawn through the ring. About 2½ inches downstream of the cascade, two total-pressure tubes and two flow-direction tubes were mounted to provide for radial surveys. The whole cascade could be rotated for tangential surveys. Static-pressure taps were located 2½ inches downstream of the cascade at the inner and outer walls. In other studies, the boundary-layer thickness on the suction surface of the blade was measured about ¼ inch from the trailing edge by means of rakes of small impact tubes. A static-pressure tube was laid against the blade. These boundary-layer measurements were made at radial positions ¼ inch from the blade root, 1$\frac{7}{32}$ inches from the outer radius, and $\frac{5}{16}$ inch from the outer radius.

Apparatus for investigation of turbine.—For over-all performance measurements, the turbine was mounted as shown in figure 6. The whole unit was inserted into a drum; the large plate at the front formed one end of the drum. The rear end of the drum was sealed by bolting the rear flange of the turbine-outlet duct to the edge of the hole in the rear plate of the drum. The entire drum was airtight except for one large port in the cylindrical surface, which served as the air inlet. The gas passed through a webbed section and the screens into the turbine.

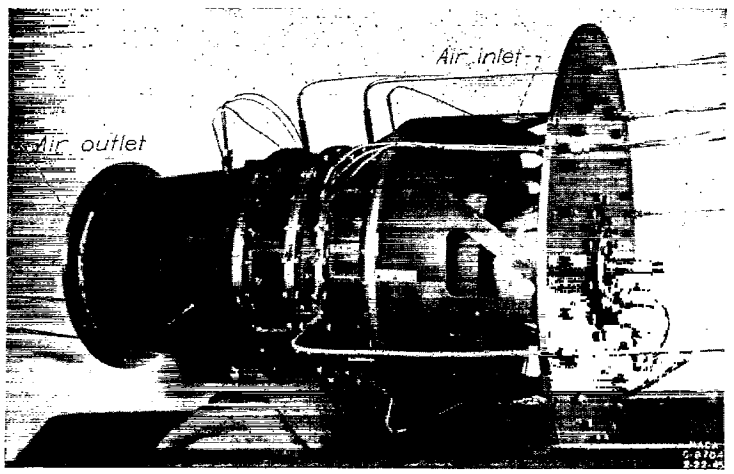

FIGURE 6.—Installation of NACA two-stage turbine for cold-air performance investigation.

The power-absorption unit was a water dynamometer. Air flow was determined from an orifice meter in the intake line. Total-pressure and temperature surveys were made upstream and downstream of the turbine by means of total-pressure tubes and thermocouples with velocity-recovery heads. Turbine power output was computed from the measured decrease in temperature and rate of flow of the air.

RESULTS

PERFORMANCE OF FIRST STATOR RING

The first stator ring was investigated to determine from the boundary layer on the blade surface whether the design method satisfactorily avoided flow separation and to find from this boundary-layer survey the drag associated with this layer and its effect on turbine efficiency. A further object was to survey the velocity distribution of the gas discharged from the stator ring and to find its effect on turbine performance. These measurements were used to evaluate the turbine-design procedure and to suggest improved procedures when disagreement existed between theoretical and measured velocity distribution.

Blade-surface boundary-layer survey.—The boundary-layer surveys on the convex side of the blade at the trailing edge are shown in figure 7. For comparison, the momentum

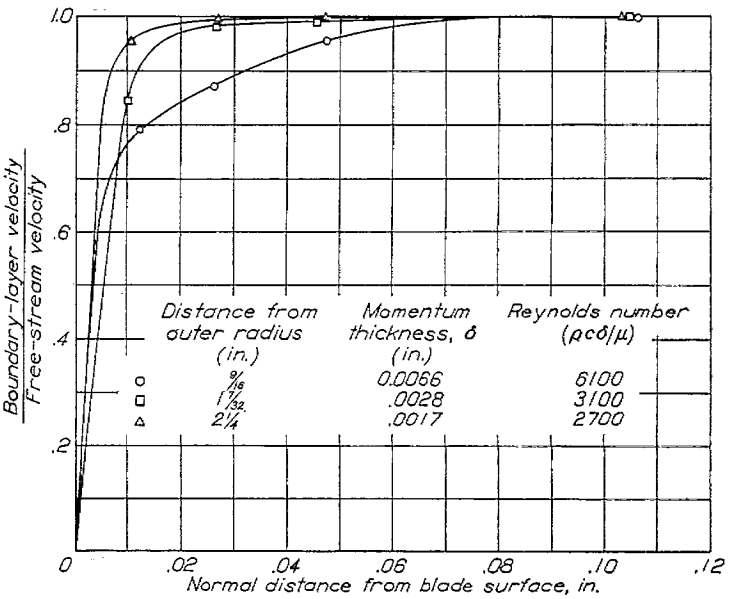

FIGURE 7.—Velocity distribution in boundary layer on blade surface ¼ inch from trailing edge of stator blade.

thickness was also computed for a turbulent boundary layer on a flat plate of chord equal to the suction-surface arc length. For all blade sections, the equivalent flat-plate boundary-layer thickness was about 0.0037 inch, which is near the average measured value for the whole blade. Because a trailing-edge thickness of 0.030 inch was required to prevent warpage of the blades under heat, the increment in drag caused by the momentum thickness of the boundary layer is small. From the momentum equation, the formula for energy loss in the blade wake is

$$\text{loss per slug} = \int T\,dS \approx \frac{\frac{c_a^2}{2}\left(\frac{t_f}{1-t_f}\right)^2}{1-\frac{c_a^2}{RT}\left[1-\frac{\gamma-1}{\gamma(1-t_f)}\right]}$$

where

t_f fraction of axial-flow area blocked by trailing edges of blades, $\frac{t}{s\cos\varphi_N}$

t blade trailing-edge thickness plus momentum thickness of boundary layer, (ft)

s blade pitch, (ft)

φ_N angle between trailing edge and normal to cascade axis

R gas content, (ft-lb/(slug)/(°R))

γ ratio of specific heats

This equation is derived in appendix B.

Computation for operation at the design point at the root-mean-square radius gives a value of $\int T\,dS$ of 160 foot-pounds per slug for an assumed boundary-layer thickness of 0.0040 inch. For a rough estimate of the effect of the blade

wake on turbine efficiency, the average value of $\int TdS$ would be about 200 foot-pounds per slug (because of the increase of c_a^2 through the turbine) if the blades were the same for all stages. Because of the varying number of blades in each stage, $\int TdS$ is approximately equal to 2100 foot-pounds per slug for the five sets of blades. Because the design work output is 1.255×10^6 foot-pounds per slug, the loss in turbine efficiency based on this factor is

$$\frac{2100}{1.255\times10^6}=0.002$$

Inasmuch as this computation shows very little effect of blade wake on turbine efficiency, the method of blade-section design is considered satisfactory.

Flow-direction surveys.—Direction-survey data for 10 measurements in a space equal to one blade pitch are shown in figure 8; the surveys were made simultaneously over opposite sides of the cascade ring. On each plot the design angle of flow for that radius is shown; the difference in average angle obtained in surveys on opposite sides of the cascade may result from variations in blade spacing and orientation. Near the inner radius (fig. 8 (a)), the air is turned too far whereas at a radius of 0.448 foot (fig. 8 (b)) the air is insufficiently turned. From a radius of about 0.5 foot to a radius of 0.542 foot, the turning is about 1° too low. Figure 9 shows surveys around a sector of the cascade; each station is removed from the next by one blade space. At the inner and outer radii, variations as high as 4° around the annulus are present. The radial distribution of turning-angle discrepancies observed in the surveys over single blade spaces are present in the survey over the whole ring. Both surveys show that the assumption of flow-direction distribution corresponding to the free-vortex condition is inadequate for an accurate description of the flow.

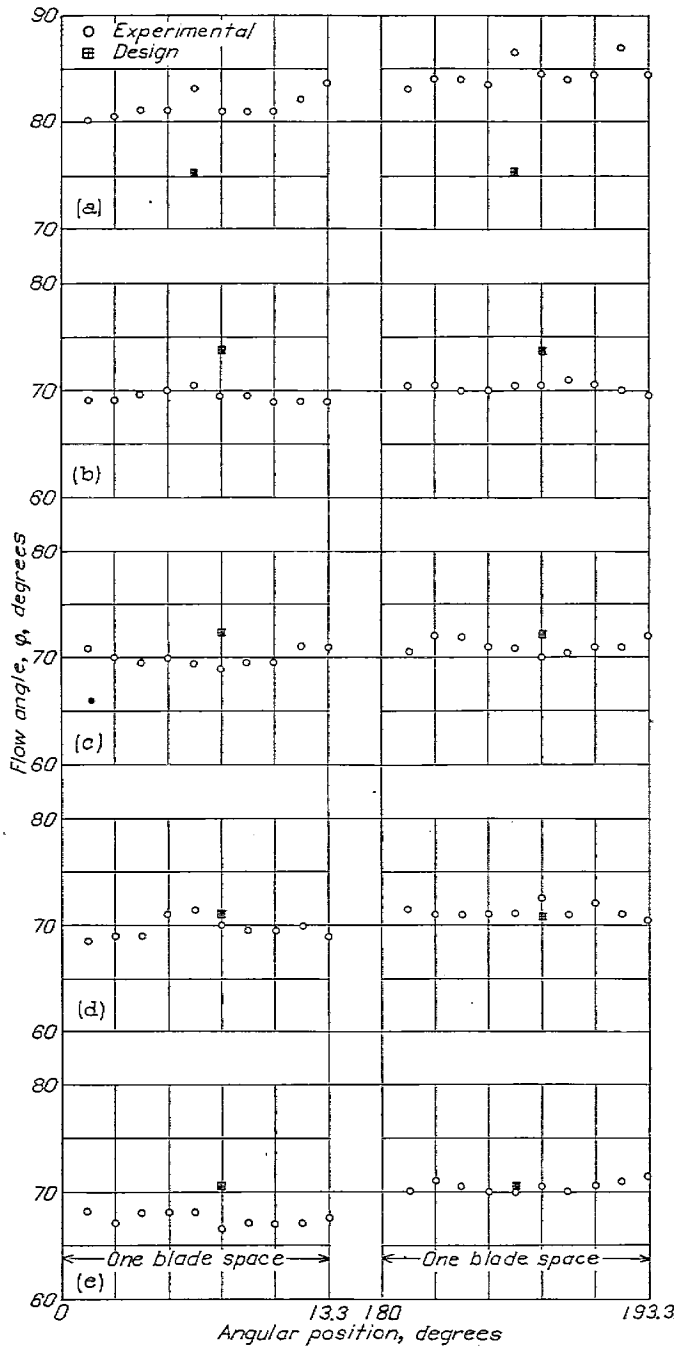

(a) Radius, 0.401 foot.
(b) Radius, 0.448 foot.
(c) Radius, 0.490 foot.
(d) Radius, 0.530 foot.
(e) Radius, 0.542 foot.

FIGURE 8.—Flow-direction surveys in first stator ring.

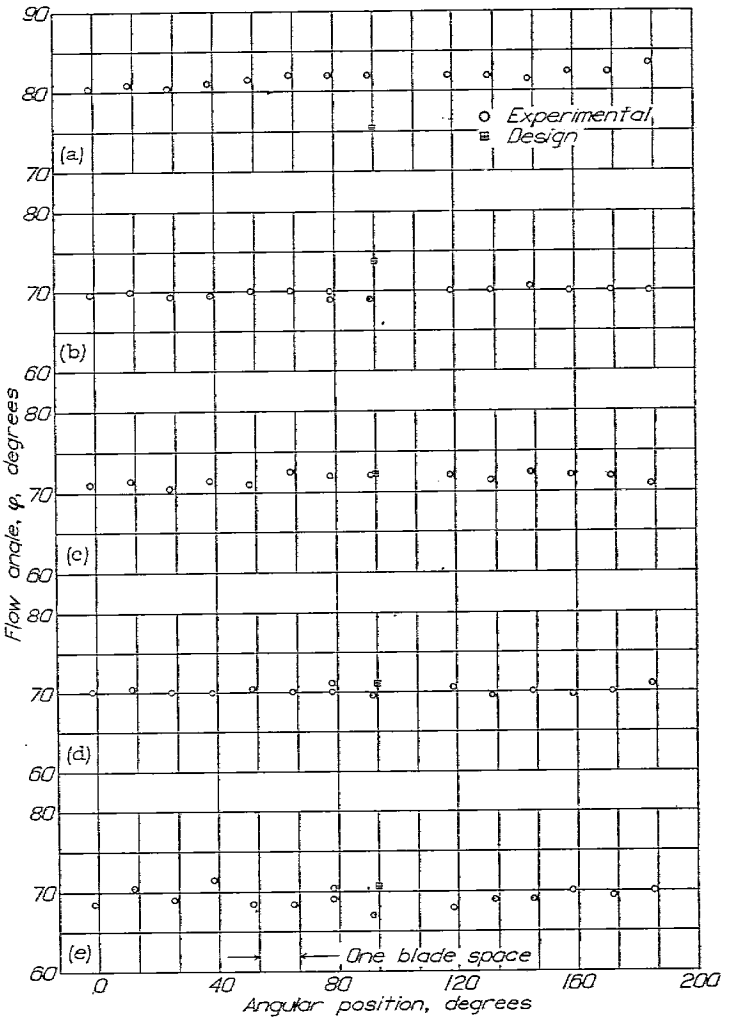

(a) Radius, 0.401 foot.
(b) Radius, 0.448 foot.
(c) Radius, 0.490 foot.
(d) Radius, 0.530 foot.
(e) Radius, 0.542 foot.

FIGURE 9.—Flow-direction surveys over sector of first stator ring.

Velocity distributions.—The gas velocities were computed on the assumption of radial equilibrium. This condition can be stated as

$$dp=\rho\frac{c_u^2}{r}dr=\gamma p\frac{c_u^2}{a^2}\frac{dr}{r}$$

where a is the local sonic velocity in feet per second. Because

$$\frac{c_u^2}{\sin^2\varphi}=c^2=\frac{2}{\gamma-1}a^2\left[\left(\frac{p_T}{p}\right)^{\frac{\gamma-1}{\gamma}}-1\right]$$

a substitution gives

$$\frac{dp}{p}=\frac{2\gamma}{\gamma-1}\left[\left(\frac{p_T}{p}\right)^{\frac{\gamma-1}{\gamma}}-1\right]\sin^2\varphi\frac{dr}{r}. \quad (5)$$

where φ is the angle between flow direction and normal to cascade axis. The data obtained in the surveys were the radial distribution of the flow direction φ and of the total pressure p_T. The static pressure was obtained at the inner and outer radii. Thus φ and p_T as functions of r and the two boundary values for p are known. If the Picard method of successive approximations is used, the solution is obtained by assuming a function $p(r)$, inserting it into the right side, integrating to get a new function $p(r)$, and repeating with the new $p(r)$. The initial point chosen was (r_r, p_r), where the subscript r indicates the inner radius. This solution, however, results in a value for the static pressure at the outer radius p_t that does not agree with the measured value. Because the total-pressure measurements were obtained with a claw tube, interference between the tubes made the total-pressure readings less reliable than the direction and static-pressure measurements. The equation was therefore used to compute the shape of the pressure-gradient curve, all values of which were then multiplied by the same factor that made $\int dp/p=\log p_t/p_r$ equal to the measured value. The values of c_u^2/a^2 obtained by use of equation (5) were used with the measured values of φ to compute the axial-velocity component. For a perfect isentropic, isoenergetic fluid passing through a cascade of blades so designed that r tan φ is constant (for this row of stator blades r tan φ= 1.535 ft), the value of c_a and rc_u are constant over the radius regardless of the flow Mach number if the flow follows the desired direction and if radial equilibrium is established.

The axial-velocity distributions are shown in figure 10 as a function of radius for several rates of air flow. The thick, low-energy layer near the inner shroud corresponds to the region of overturning noted in the direction surveys. Next to this region is a local region containing a velocity maximum. This region of extreme underturning was noted in the direction surveys. The boundary layer on the outer shroud is quite thin. The plot of moment-of-momentum parameter rc_u/a_T (fig. 11) shows the same thick inner boundary layer and thin outer boundary layer. The region of high axial velocity does not have a corresponding region of high moment of momentum, which explains the underturning in this region. This discrepancy between excessive axial-velocity component and low moment of momentum means that the flow into this region from the inner shroud, and hence the build-up of the boundary layer, did not take place mainly inside the blade channels where it would cause an increase in rc_u, but primarily occurred outside the nozzle channel.

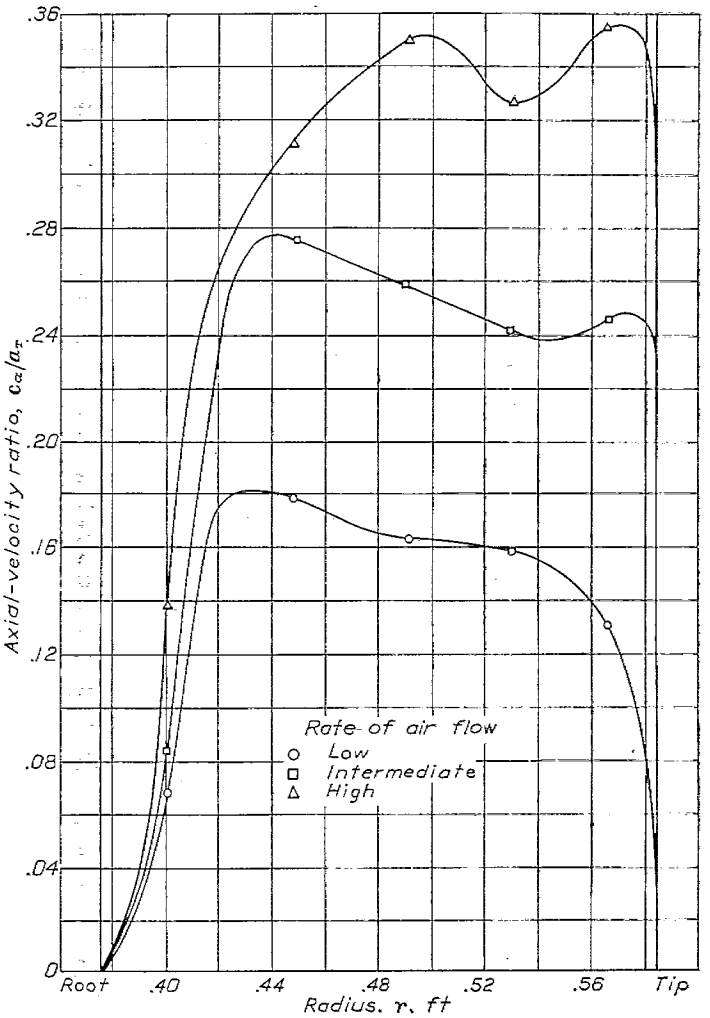

FIGURE 10.—Radial distribution of axial velocity downstream of first stator ring.

An increase in low-energy region on the inner shroud occurs with increase in mass flow. Because all flows are subsonic, it is assumed that this is a Reynolds number effect. For high flows dynamically similar to low flows

$$\rho_h c_h L_h=\rho_l c_l L_l$$

and

$$\rho_h c_h>\rho_l c_l$$

where L is the characteristic length and the subscripts h and l indicate the high-flow and low-flow conditions, respectively. The distance behind the blades rather than the blade height is selected as L because the viscous effects do not extend from the inner to the outer shroud, although this state is almost attained at the highest flow. The conditions just cited imply that $L_h<L_l$, which means that the surveys taken at high flows correspond to the low-flow surveys taken farther downstream. This interpretation is useful because the data for various flows at one position may be interpreted as corresponding to the same flow at various survey planes. This interpretation is not exact because dynamic similarity implies geometric similarity, which is not maintained in the blade sections.

Physical interpretation of velocity and direction distribution.—A change from potential flow occurs near the blade shrouds because of the large viscous forces. The concave surface of the blade is a high-pressure region and the convex surface is a low-pressure region (A-B, fig. 1) that extends beyond the channel between the blades. In the main body of the flow (the region not near the blade root nor tip), the momentum is high enough to carry the flow in a direction transverse to the pressure gradient. Adjacent to the inner and outer shrouds is a region of low momentum induced by friction with these walls and by turbulent and viscous shearing stresses. This low-momentum fluid flows almost directly in the direction of the pressure gradient induced by the potential flow on the blade surfaces. The velocity of these low-energy boundary layers at the shrouds has a component opposed to the main axial-flow component, and also a component in the direction of rotation of the main body of the fluid. This boundary layer at the shrouds is therefore built up after discharge from the channel section B-C, (fig. 1) although some build-up may take place inside the channel. This layer of air will therefore appear to be overturned (fig. 8) even though both velocity components are low. The build-up of this boundary layer at the shrouds causes a radial flow, which in turn induces a high axial velocity in an adjacent local region (fig. 10), and thus the air is underturned (fig. 8) although its tangential component may be equal to the design value.

A radical difference is noted in the thickness and the thickness development with velocity of the boundary layers on the inner and outer shrouds (figs. 10 and 11). It may be simply demonstrated that this effect is caused by the stability of the inner boundary layer and the instability of the outer layer. The radial accelerating force on a fluid element of mass $\rho dr\ rd\lambda$ is the difference between the centrifugal force $(\rho dr\ rd\lambda)\ c_u^2/r$ and the pressure-gradient force:

$$\left(p+\frac{dp}{dr}\,dr\right) rd\lambda - prd\lambda = \frac{dp}{dr}\,dr\ rd\lambda$$

where $rd\lambda$ is an element of length along cascade axis at radius r. The radial force per unit mass is then $\frac{(rc_u)^2}{r^3}-\frac{1}{\rho}\frac{dp}{dr}$.

A stable rotating body of fluid has a net radial force of zero everywhere. If a particle of fluid at position r with moment of momentum rc_u is displaced to a position r_d where the prevailing moment of momentum is $(rc_u)_d$ and where equilibrium establishes a pressure gradient of

$$\frac{1}{\rho_d}\left(\frac{dp}{dr}\right)_d = \frac{(rc_u)_d^2}{r_d^3}$$

then according to the principle of conservation of momentum the particle will retain its original moment of momentum. The unbalanced force per unit volume on the particle in its new position in the pressure field therefore is

$$\frac{\rho(rc_u)^2}{r_d^3} - \left(\frac{dp}{dr}\right)_d = \frac{\rho(rc_u)^2 - \rho_d(rc_u)_d^2}{r_d^3}$$

If a particle from the low-velocity boundary layer is displaced radially to a region of higher moment of momentum, the resulting force on the fluid is negative and tends to send the particle inward. The stability of the inner boundary layer and the instability of the outer boundary layer are thereby explained. Furthermore, any particles of fluid in the main stream that have a low moment of momentum (such particles may come from the blade wake or from the boundary layer of the outer shroud) also tend to collect along the inner shroud, thus building up this boundary layer at a greater rate than by friction alone.

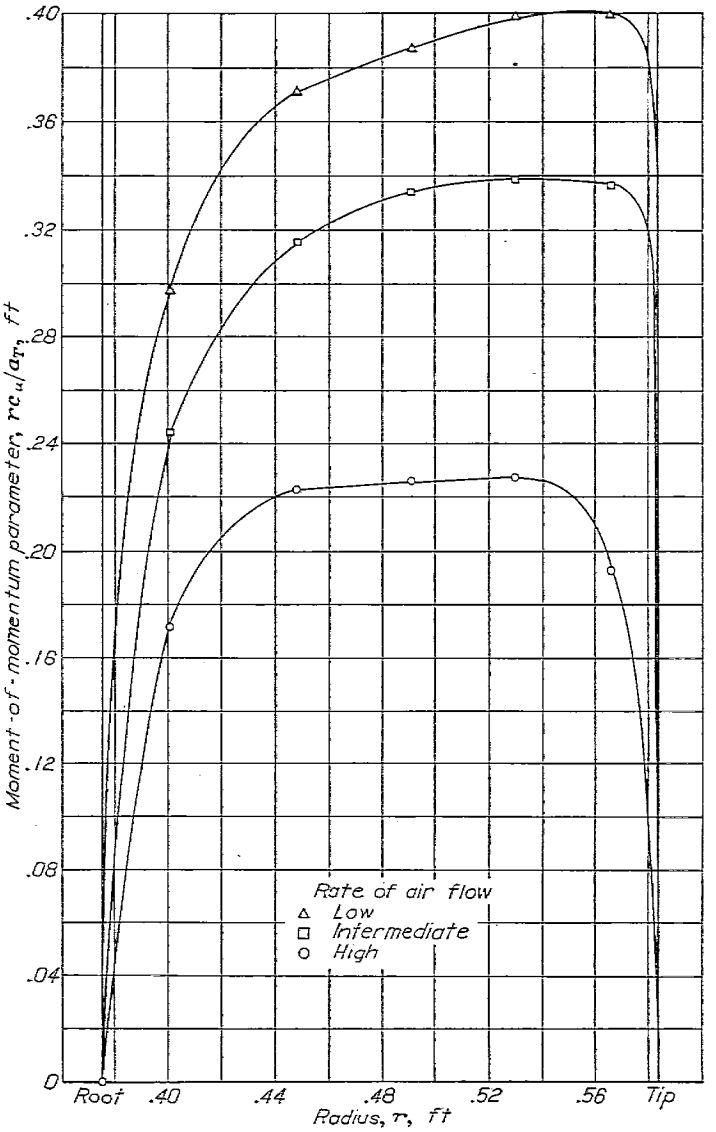

FIGURE 11.—Radial distribution of moment of momentum downstream of first stator ring.

This reasoning is supported by figure 10, which shows a thick inner layer and a thin outer layer. As predicted, the inner boundary layer builds up and the outer layer thins out with increasing velocity (which corresponds to increasing distance from the cascade). The same general character is shown in the curves of the moment of momentum (fig. 11). For a rotating inner shroud, the boundary layer is therefore unstable, whereas, for the rotating outer shroud, the layer is stable. A minimum thickness in all boundary layers is therefore obtained by having a rotating inner shroud and a stationary outer shroud as in the compressor component of the engine for which this turbine was designed.

Relation of cascade performance to design and turbine performance.—The purpose of the cascade is to impart a desired moment of momentum to the air. For turbine power, the radial distribution of moment of momentum is not as significant as the mass distribution of the moment of momentum, which is shown in figure 12. The weight flow

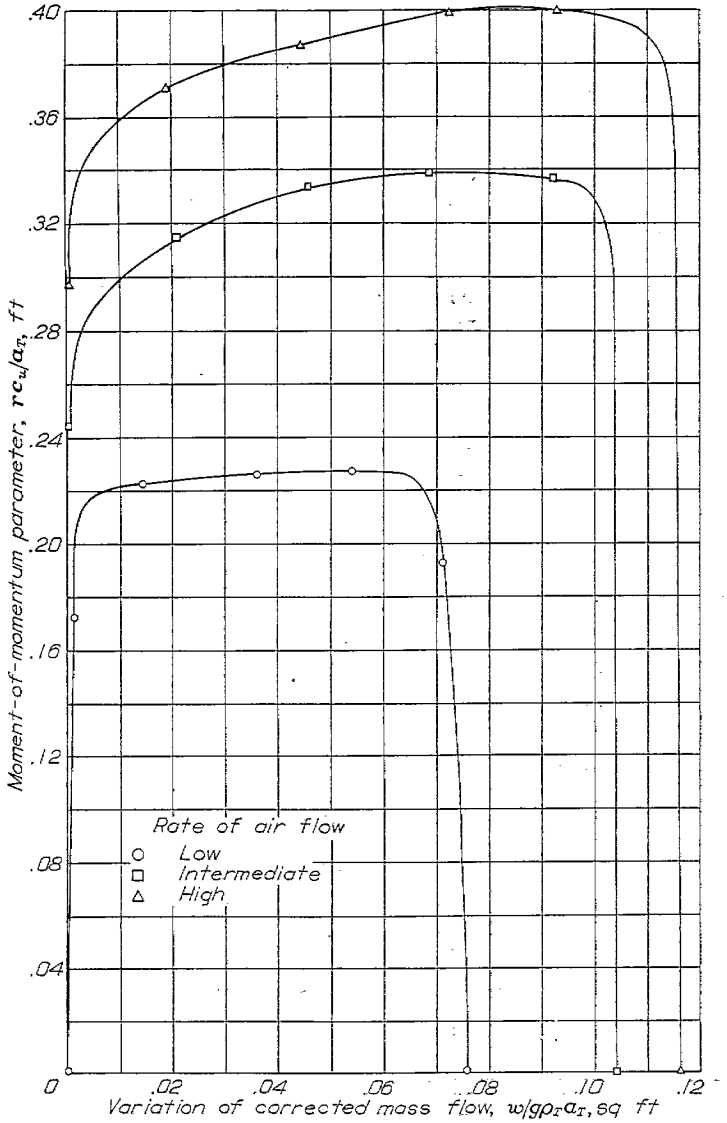

FIGURE 12.—Mass distribution of moment of momentum downstream of first stator ring.

w between the inner shroud and a radius r is therefore a function of r. The curves are more nearly constant than the curves of figure 11, showing a very steep rise from zero at both shrouds. The design value of the mass-flow parameter $W/g\rho_{T,3}\,a_{T,3}$ is 0.0723 square foot, slightly lower than the lowest test condition, which was 0.0757 square foot. (W, total weight flow through the stator blades, lb/sec; g, gravitational factor; subscript 3 indicates state of air entering the first set of stator blades.) In order to compare measured values of rc_u with design values, use is made of the fact that, for a perfect fluid, if rc_u and the energy are constant for one flow, rc_u and c_a are constant over the radius for any other flow and rc_u/c_a is constant for all flows and radii with constant angle distribution and radial equilibrium. The mass-averaged $\bar{c}_a$ was computed and the parameter $rc_u/\bar{c}_a$ was plotted against the corrected variation in mass flow $w/g\rho_{T,3}\,a_{T,3}$ in figure 13, which shows that the effective angle of turning is smaller than the design angle.

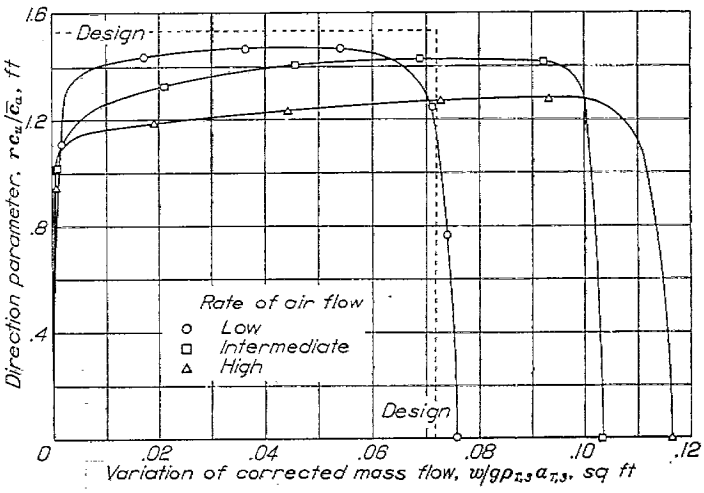

FIGURE 13.—Mass distribution of direction parameter $rc_u/\bar{c}_a$.

In order to estimate the weight flow at the design pressure drop, use is made of the fact that for this turbine, the corrected weight flow as a function of pressure ratio is independent of speed. Because of subcritical flows the pressure ratio over the nozzle is a function only of the mass-flow parameter, which in turn is a function of the turbine over-all pressure ratio and independent of speed, the pressure ratio of the first stator is therefore a function of the pressure ratio of the whole turbine and is independent of speed. For this turbine, the relation of weight flow and pressure drop for design conditions can be computed either from conditions at the root-mean-square radius $\sqrt{\frac{1}{2}(r_t^2+r_i^2)}$ with the entire flow area or by computation and integration over the whole blade height. The pressure ratio or the corresponding $c/a_{T,3}$ at the root-mean-square radius is therefore taken as typical of this stator. The design pressure drop over the whole turbine is therefore assumed to prevail when $c/a_{T,3}$ is equal to the design value at the root-mean-square radius of the first stator.

The area of flow is blocked principally at the inner shroud. The air flow at design pressure drop is estimated by assuming an effective area determined from the experiment with the lowest flow. The actual velocity ratio

$$\frac{\bar{c}}{a_T}=\frac{1}{a_T}\sqrt{\bar{c}_a^{\,2}+\bar{c}_u^{\,2}}$$

implies a certain density ratio $\bar{\rho}/\rho_T$ for isentropic flow. The effective flow area A_e is computed from

$$\frac{W}{g\rho_T a_T}=A_e\left(\frac{\bar{\rho}}{\rho_T}\right)\left(\frac{\bar{c}_a}{a_T}\right)$$

and from the data for the lowest-flow condition. From the value of $\bar{c}/a_T$ and $\bar{\rho}/\rho_T$ for the design conditions and the effective area, the flow at design pressure ratio and standard atmospheric condition for the entering stagnation state is 5.85 pounds per second, which is 95 percent of the design value. The effective flow area is 87.5 percent of the actual value. The assumption of free-vortex flow and uniform axial velocity is therefore unsatisfactory for estimating the air-flow—pressure-ratio relation of the turbine.

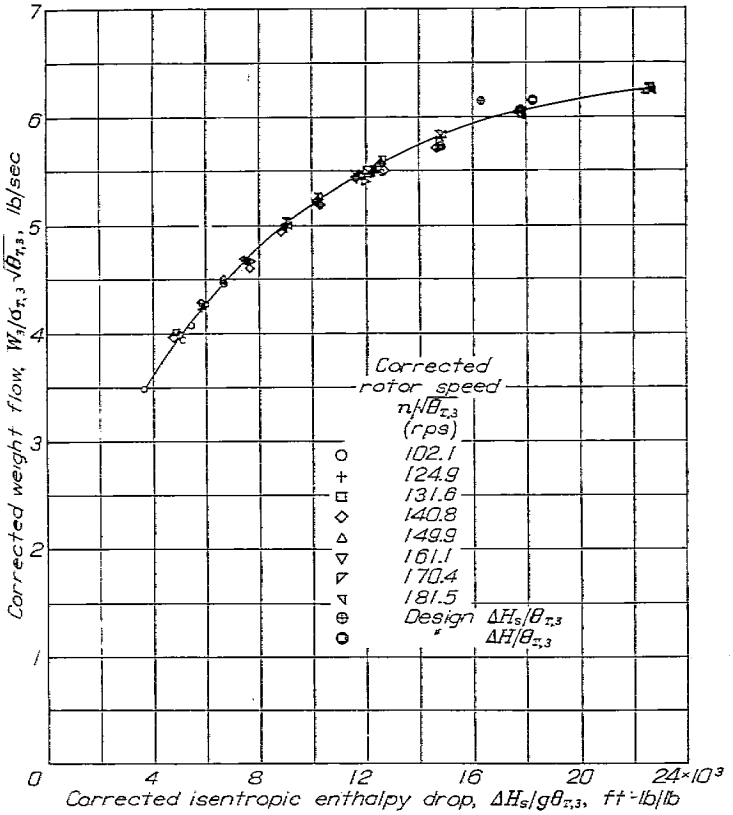

FIGURE 14.—Variation of weight flow with isentropic enthalpy drop of NACA two-stage turbine.

If the mean axial-velocity component $\bar{c}_a$ is decreased in the ratio 0.875 to account for the area blockage, then the value of $r\bar{c}_u/\bar{c}_a$ is changed from 1.348 to 1.540, which closely approximates the design value of 1.535. Thus the underturning of the air is almost exactly accounted for by the blockage of flow at the blade root with the design value of moment of momentum. This underturning may be explained by assuming that most of the build-up of the inner boundary layer takes place after discharge from the nozzle by flow toward the suction surface of the blade, which projects beyond the guided channel section. The main effect of these phenomena is to increase the axial-velocity components over the part of the blade just outside the shroud boundary layer and to reduce the air flow from the design value. The poor angle of attack at the rotor-blade roots is relatively insignificant because of the small part of the flow in that region, but the deviations from design angles are relatively significant in the potential-flow region adjacent to the inner shroud. Accurate design procedure requires the development of a method of predicting these effects near the shroud.

TURBINE PERFORMANCE

The relation between the corrected weight flow of the turbine $W_3/(\sigma_{T,3}\sqrt{\theta_{T,3}})$, the corrected turbine rotor speed $n/\sqrt{\theta_{T,3}}$, and corrected isentropic enthalpy drop $\Delta H_s/g\theta_{T,3}$ is given in figure 14 where

W weight flow of gas through compressor or turbine, (lb/sec)

σ ratio of density to normal gas density, ρ/ρ_{st}

θ square of ratio of sonic speed to sonic speed for normal air, a^2/a_{st}^2 (referred to as corrected temperature ratio because of relation

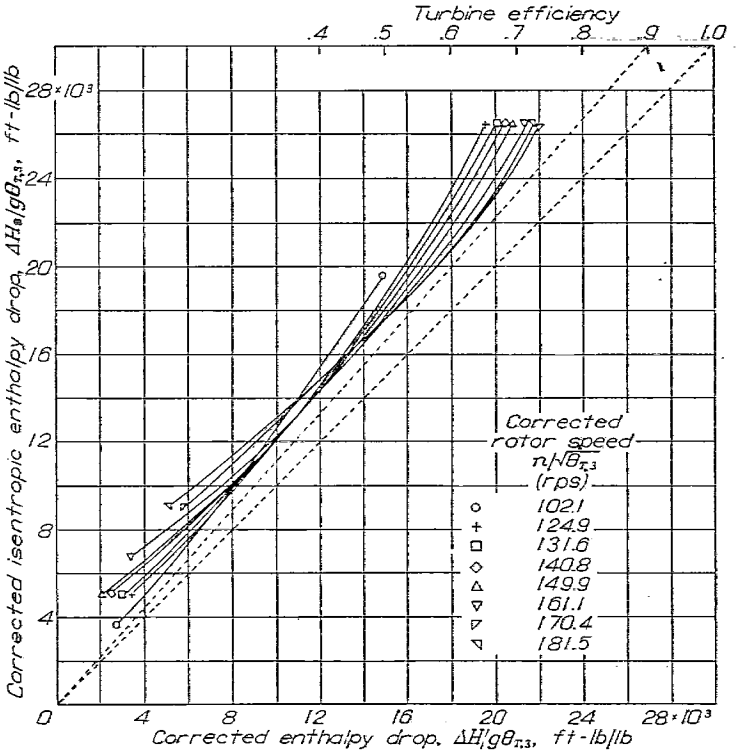

FIGURE 15.—Isentropic and actual enthalpy change through NACA two-stage turbine.

$$\theta \equiv \frac{a^2}{a_{st}^2} = \left(\frac{\gamma R}{\gamma_{st} R_{st}}\right)\left(\frac{T}{T_{st}}\right)$$

ΔH_s isentropic enthalpy drop through turbine, (ft-lb/slug)

n rotor speed, (rps)

Subscripts:

3 turbine-inlet condition

st standard-air condition

Figure 14 shows that the turbine behaves like a nozzle with no effect of rotative speed. The design point computed on the assumption of an efficiency of 0.90 is also shown. The weight flow at design pressure drop is about 96.4 percent of the design value, rather than 95 percent as predicted from the cascade performance; the agreement of flow predicted from cascade data with turbine performance is good. This increase in air flow may be caused by the influence of the rotating set of blades, which might render the inner boundary layer unstable and thus destroy it. This influence may be felt to some extent by the layer just downstream of the first row of nozzles, which becomes thinner and thus reduces the flow obstruction. Figure 15 shows the corrected isentropic enthalpy drop of the air as a function of the corrected enthalpy drop; the efficiency contours are straight dashed lines through the origin of slope equal to the reciprocal of the efficiency. A peak efficiency of 0.875 is noted. The enthalpy curves show nearly constant efficiency over a wide range of speeds and power outputs. At the design value for speed and work output per pound of air, the efficiency is 82 percent rather than 90 percent, which was used in the design process. At the corresponding isentropic enthalpy drop, which is 90/82 times the design value, the air flow is only 1.7 percent lower than the design value of 6.18 pounds per second. This design point is also shown on figure 14. When the turbine operates in the engine, it will handle slightly more gas than indicated from these data because of

the expansion of the clearances under the action of the hot gases. The agreement between design and actual air flow at design work output can therefore be regarded as satisfactory.

A plot of the over-all turbine performance in figure 16 shows a corrected torque parameter plotted against a corrected weight-flow parameter, both of which are useful in finding the matching and the interaction of the turbine and the compressor as components of a jet engine. Lines of constant corrected rotor speed and of constant turbine efficiency are shown as well as the location of the design point. The design point is not the point of highest efficiency

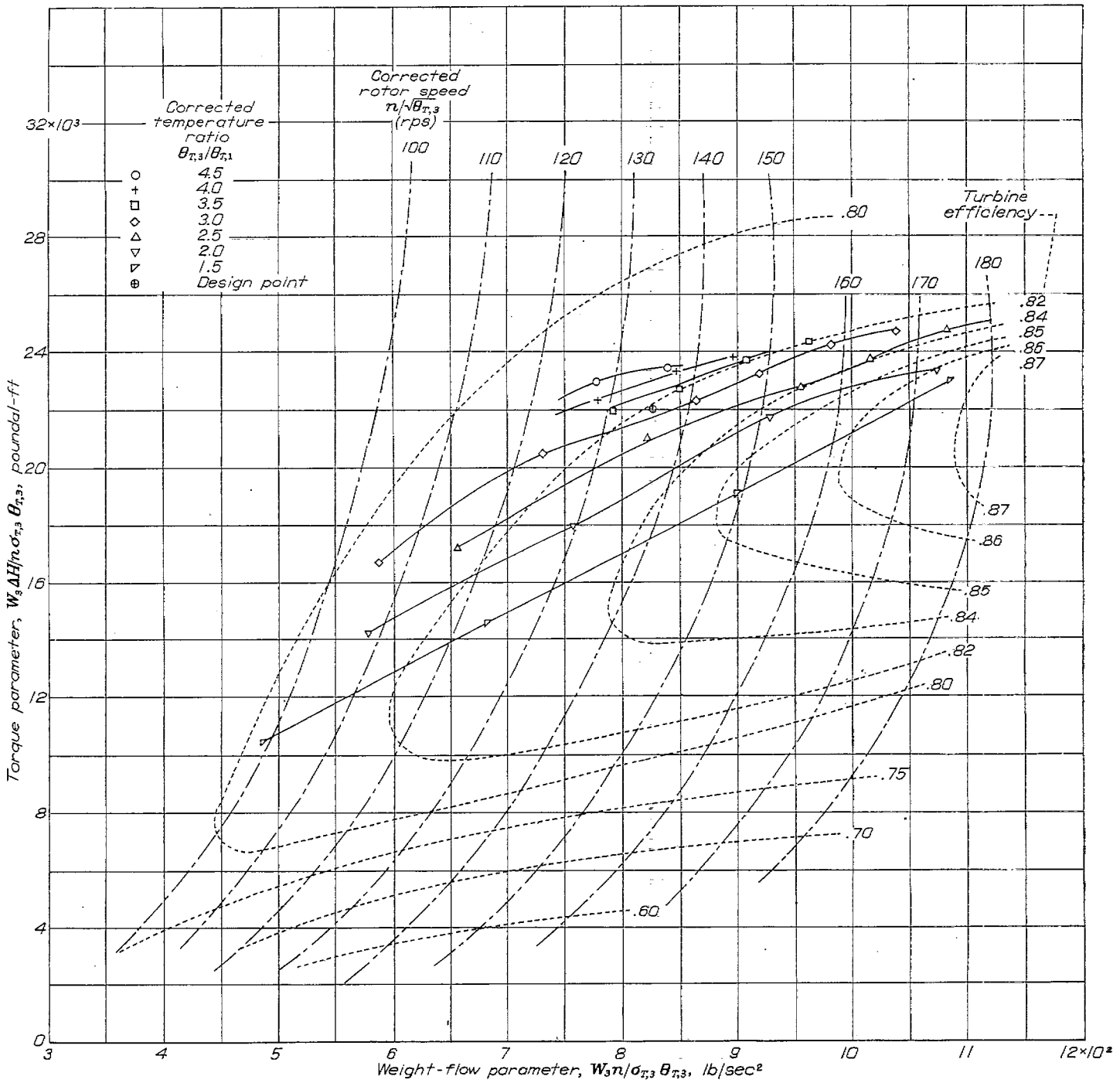

FIGURE 16.—Matching chart for NACA two-stage turbine.

inasmuch as this efficiency was about 0.823 as compared with the peak value of 0.875 at a speed of 180 revolutions per second. This discrepancy in speeds indicates that an analytical determination of efficiency is required in order to produce the most effective designs with minimum losses at the design point. A large range of high efficiency is available, however, for use at points other than the design point.

TURBINE-COMPRESSOR MATCHING

The turbine characteristics are now used to determine how well they match the characteristics of the compressor with which the turbine is to be used. The turbine may be expected to behave somewhat differently than predicted by the cold-air data when installed in the engine because of the changed properties of the working fluid, the clearance expansion, the nonuniform temperature distribution in the incoming stream, and the combustion in the turbine in some conditions of operation. Another difference may be expected because the data available for the compressor were obtained with a scroll-discharge collector rather than the axial-discharge collector that will be used in the engine. Another unknown is the combustion-chamber total-pressure loss, which is assumed to be 5 percent of the absolute total pressure delivered by the compressor.

RELATION BETWEEN TURBINE AND COMPRESSOR VARIABLES

The matching of the turbine and compressor components of the engine is determined by related parameters of the compressor and the turbine. For example, the speed of the turbine is equal to that of the compressor and the relation between the equivalent speeds is

$$\frac{n}{\sqrt{\theta_{T,1}}}=\frac{n}{\sqrt{\theta_{T,3}}}\sqrt{\frac{\theta_{T,3}}{\theta_{T,1}}} \tag{6}$$

where the subscript 1 indicates state at compressor inlet.

Compressor and turbine gas flows are related by the equation

$$W_3=(1+f)W_1$$

where f is the fuel-air ratio. Then

$$\frac{W_1 n}{\sigma_{T,2}\theta_{T,2}}=\frac{1}{1+f}\frac{W_3 n}{\sigma_{T,3}\theta_{T,3}}\frac{\sigma_{T,3}}{\sigma_{T,2}}\frac{\theta_{T,3}}{\theta_{T,2}}$$

where the subscript 2 indicates state at the compressor outlet.

Because

$$\sigma_{T,2}\theta_{T,2}=\frac{\gamma_2 p_{T,2}}{\gamma_{st}p_{st}}$$

and

$$\sigma_{T,3}\theta_{T,3}=\frac{\gamma_3 p_{T,3}}{\gamma_{st}p_{st}}$$

then

$$\frac{W_1 n}{\sigma_{T,2}\theta_{T,2}}=\frac{\gamma_3 p_{T,3}}{\gamma_2 p_{T,2}(1+f)}\frac{W_3 n}{\sigma_{T,3}\theta_{T,3}} \tag{7}$$

which relates the turbine and compressor gas flows in terms of parameters that are reduced to standard-air values.

The power equation is

$$W_1(H_{T,2}-H_{T,1})+P_A=W_3(H_{T,3}-H_{T,4})$$

or

$$W_1\Delta H_c+P_A=W_3\Delta H$$

where

P_A auxiliary-power consumption (bearings), (ft-lb/sec)
ΔH enthalpy drop through turbine, $H_{T,3}-H_{T,4}$

This equation can be converted into a relation between the compressor and turbine torques in equivalent variables:

$$\frac{W_1\Delta H_c}{n\sigma_{T,2}\theta_{T,2}}+\frac{P_A}{n\sigma_{T,2}\theta_{T,2}}=\left(\frac{W_3\Delta H}{n\sigma_{T,3}\theta_{T,3}}\right)\frac{\sigma_3\theta_{T,3}}{\sigma_{T,2}\theta_{T,1}}=\left(\frac{p_{T,3}}{p_{T,2}}\right)\frac{\gamma_3}{\gamma_2}\left(\frac{W_3\Delta H}{n\sigma_{T,3}\theta_{T,3}}\right) \tag{8}$$

For the combustion chamber, the pressure-loss function is assumed to be in the form

$$\frac{p_{T,2}-p_{T,3}}{p_{T,2}}=\text{function of}\left(\frac{W_1^2}{\rho_{T,2}p_{T,2}},\ W_1,\ f\right) \tag{9}$$

and the combustion efficiency

$$\eta=\frac{W_3H_{T,3}-W_1H_{T,2}-fW_1H_b}{W_1fh} \tag{10}$$

is given as

$$\begin{aligned}\eta&=\text{function of }(H_{T,3},\text{ conditions at station 2})\\&=\text{function of }(f,\text{ conditions at station 2})\end{aligned} \tag{11}$$

where

H_b enthalpy of fuel entering combustion chamber, (ft-lb/slug)

h heating value of fuel, (ft-lb/slug)

COMPRESSOR AND TURBINE MATCHING CHARTS

Except for small corrections for fuel input, bearing power, pressure loss in the combustion chamber, and change in γ from station 1 to station 4, the torque parameter $W\Delta H/(n\sigma\theta)$ equation (8) is the same for the turbine and for the compressor under any engine operation condition. The same equality holds for the air-flow parameter $Wn(\sigma\theta)$, as equation (7) shows. If the turbine and compressor performances are plotted in terms of these variables and the charts superimposed, one point indicates both the turbine and compressor

operating states when they are operating as components of a jet engine. A chart of the compressor performance in terms of these variables is shown in figure 17 for constant values of $n/\sqrt{\theta_{T,1}}$. These data for the compressor with a scroll collector were obtained from references 2 and 3. Some difference is to be expected between the performance so determined and the performance of the compressor when straightening vanes are substituted for the scroll for use in the engine. A similar chart for the turbine is shown in figure 16 for constant values of $n/\sqrt{\theta_{T,3}}$. If the charts for the turbine and the compressor are superimposed, it can be seen whether the high-efficiency region for the turbine overlaps the high-efficiency region for the compressor. If they do not, the resultant jet engine is prevented from reaching its maximum possible efficiency.

The over-all engine performance can also be estimated from these charts, and the relation of each component to the over-all engine performance can be determined. This relation will indicate the most appropriate modifications of turbine and compressor to obtain better over-all engine performance. First, a rough approximation is made by assuming no bearing losses, no combustion-chamber pressure loss, and no fuel added. If a value for the corrected temperature ratio $\theta_{T,3}/\theta_{T,1}$ is assumed, the ratio of turbine to compressor speed is fixed for this value of $\theta_{T,3}/\theta_{T,1}$ by equation (6). By superimposing the two charts and choosing a particular compressor-speed line, the intersection of this line with a turbine-speed line having the correct ratio of turbine speed to the compressor speed determines an engine operation point. The choice of another compressor speed determines another point. In this manner, an operation curve can be obtained for each temperature ratio. The flow and the state of the air discharged from the compressor can then be obtained for each operating point. The engine characteristics are now refined to take into account losses and changes in gas properties. The bearing power P_A may be found from the operation speed. Then approximately

$$f \approx \frac{(H_{T,3}-H_{T,1})-\Delta H_c}{\eta h-(H_{T,3}-H_{T,1})} \tag{12}$$

From the data on the compressor-discharge and burner characteristics, η and f can be computed from equation (11). This value of f with $\theta_{T,3}/\theta_{T,1}$ and $\theta_{T,1}$ permits the determination of γ_3/γ_1 and $T_{T,3}/T_{T,1}$. Sufficient data are then available to find the value of $p_{T,3}/p_{T,2}$.

The turbine torque and air-flow requirements may now be computed to include the effect of compressor, combustion-chamber pressure loss and efficiency, and bearing requirements by the application of equations (7) and (8) for several points on each compressor-speed curve. These points are connected by a curve for a given speed. The intersection of these curves of turbine requirements with the proper speed curves of turbine performance gives turbine operating points that can be corrected by equations (7) and (8) to give the corresponding compressor operating points. These results should be of the desired accuracy but should be checked to see that they fall on the original compressor curve. Equation (12) is used with the burner chart (equation (11)) to find f. A check on the accuracy can be made by recomputing the intersection points with the new value for f and improved values for the bearing correction and $p_{T,3}/p_{T,2}$. In the example being computed, it was assumed that $\eta=0.9$ and $p_{T,3}/p_{T,2}=0.95$. The bearings were assumed to use a torque of 7 inch-pounds and the compressor-inlet conditions corresponded to an altitude of 30,000 feet and a flight speed of 470 miles per hour.

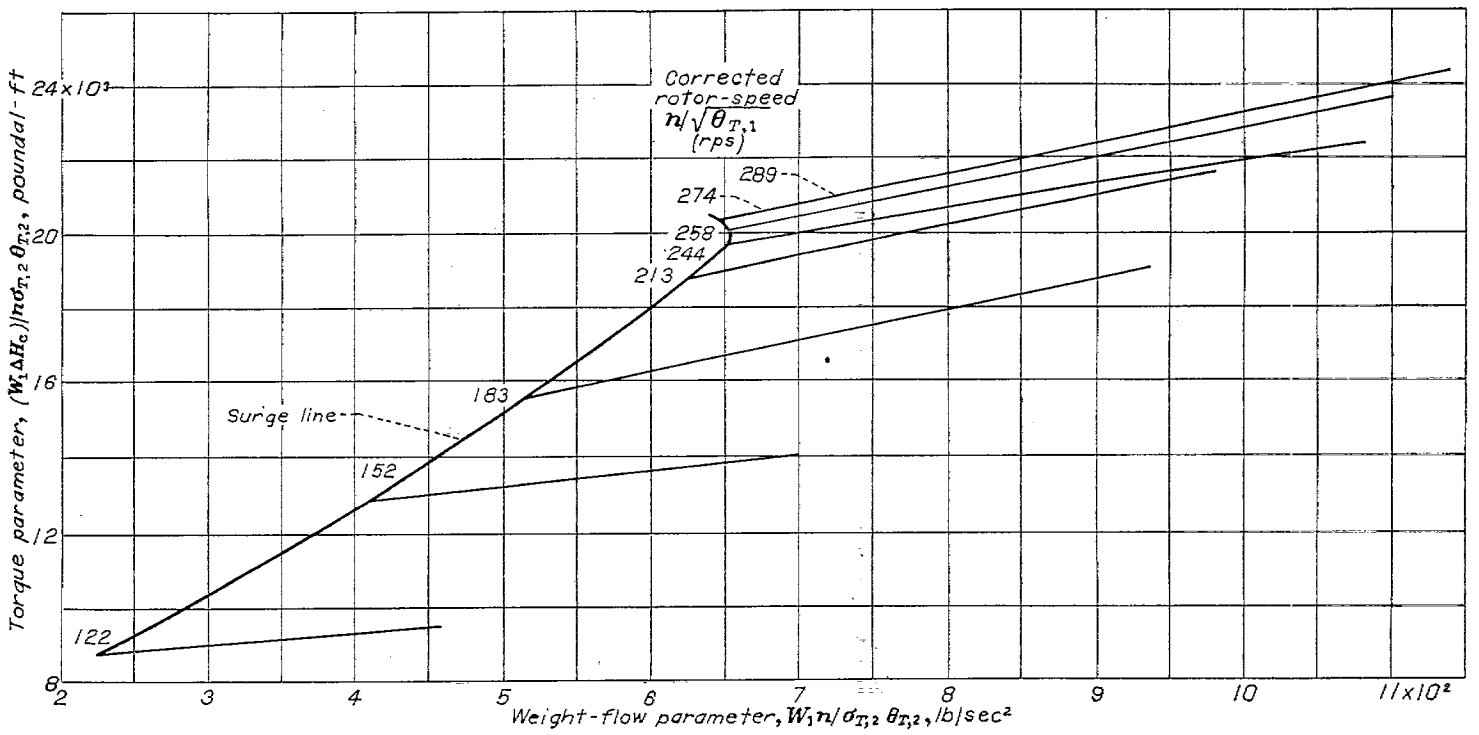

FIGURE 17.—Matching chart for NACA eight-stage compressor. (Data from references 2 and 3.)

The compressor-operation curves for constant corrected temperature ratio $\theta_{T,3}/\theta_{T,1}$ are shown in figure 18 and the corrected temperature-ratio lines are shown on the turbine chart (fig. 16). The compressor and the turbine are not perfectly matched as shown in figure 16 by the fact that none of the $\theta_{T,3}/\theta_{T,1}$ lines pass through the region of maximum turbine efficiency. The highest compressor efficiency is being used when $\theta_{T,3}/\theta_{T,1}=3.5$ and $n/\sqrt{\theta_{T,1}}=274$ revolutions per second. Under these conditions the turbine is operating at an efficiency of only 0.82. These operation curves cover all modes of operation of the engine with arbitrary ram and exhaust pressures and discharge-jet nozzle sizes, but only a small part of the entire turbine performance range of good efficiency. Data obtained from experiments with this jet engine as a complete unit therefore cannot be expected to cover a range large enough to indicate where the region of peak turbine efficiency is and whether the components are well matched.

The effect of the discrepancies between design estimates and turbine performance on engine operation is minor insofar as the compressor-operation states are concerned, because of good correlation between air flow estimated and measured at the design value for turbine work per pound of air at design speed. These three variables are enough to determine that the compressor will operate at design air-flow conditions for the desired speed and temperature ratio. Because the turbine pressure ratio is not close to the estimated value under these circumstances (measured efficiency, 0.82; design efficiency, 0.90), less pressure will be available for the jet nozzle, which must therefore be larger than first estimated.

JET-ENGINE PERFORMANCE COMPUTATIONS

In order to compute the jet-engine performance at a given altitude and speed, the ram pressure (generally corrected for duct losses but not in this example) and the temperature at the compressor inlet are computed and from them $V/\sqrt{\theta_{T,1}}$ and $p_{T,1}/p_0$ are determined. The flight speed is V and p_0 is the free-stream pressure. If the subscript 4 indicates turbine-outlet state, then the jet pressure ratio may be written

$$\frac{p_{T,4}}{p_0}=\frac{p_{T,1}}{p_0}\frac{p_{T,4}}{p_{T,1}}$$

where $p_{T,4}/p_{T,1}$ is presumed known from previous engine computations. If the values of γ_4 and $T_{T,4}$ are known, the corrected jet velocity $c_5/\sqrt{\theta_{T,1}}$ may be computed from

$$\frac{c_5}{\sqrt{\theta_{T,1}}}=a_0\sqrt{\frac{\theta_{T,4}}{\theta_{T,1}}}\sqrt{\frac{2}{\gamma_4-1}}\left[1-\left(\frac{p_0}{p_{T,4}}\right)^{\frac{\gamma_4-1}{\gamma_4}}\right]^{\frac{1}{2}} \text{(ft/sec)}$$

where the subscript 5 indicates propulsion-nozzle conditions.

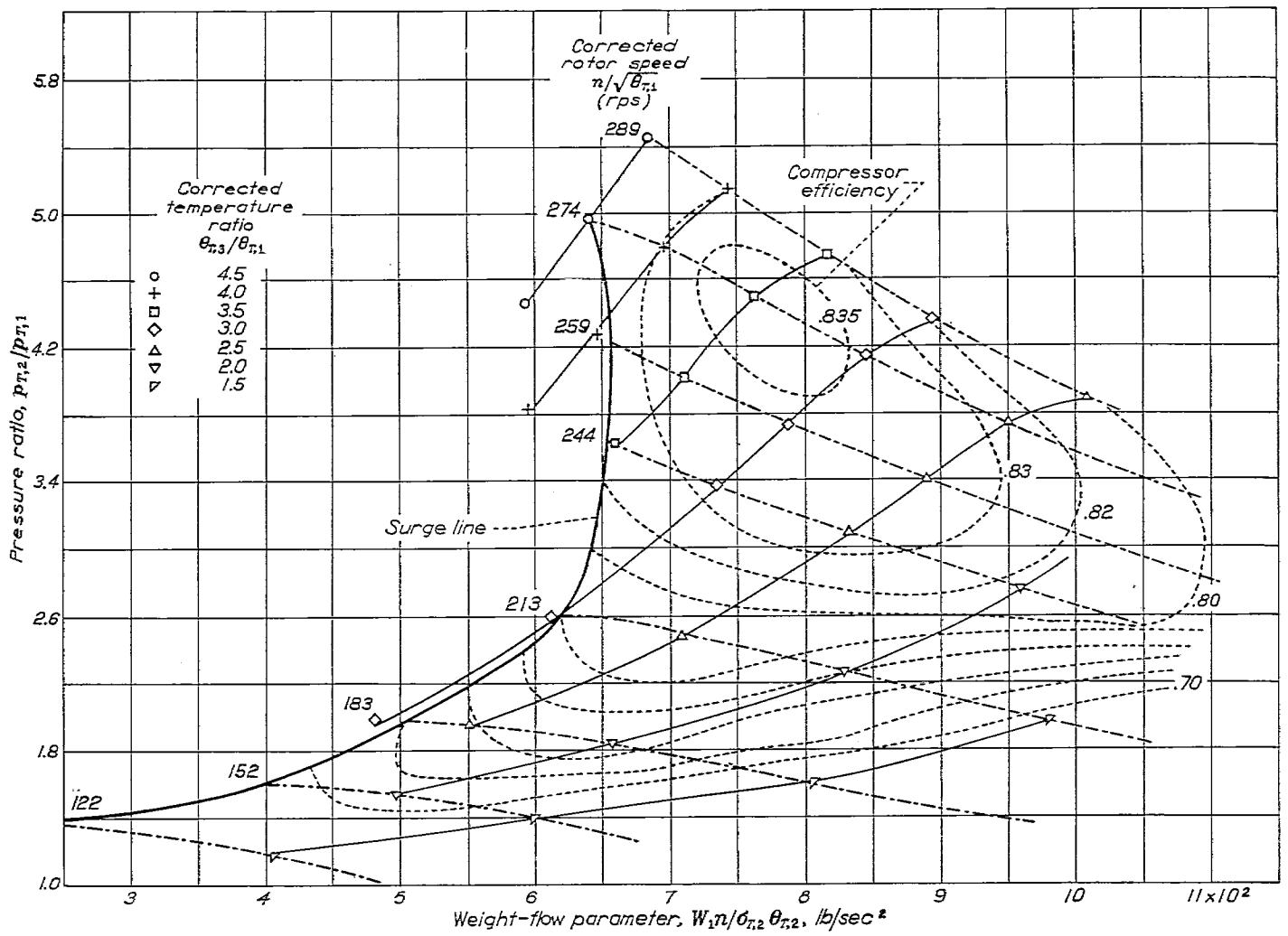

FIGURE 18.—Estimated operation of compressor in jet engine.

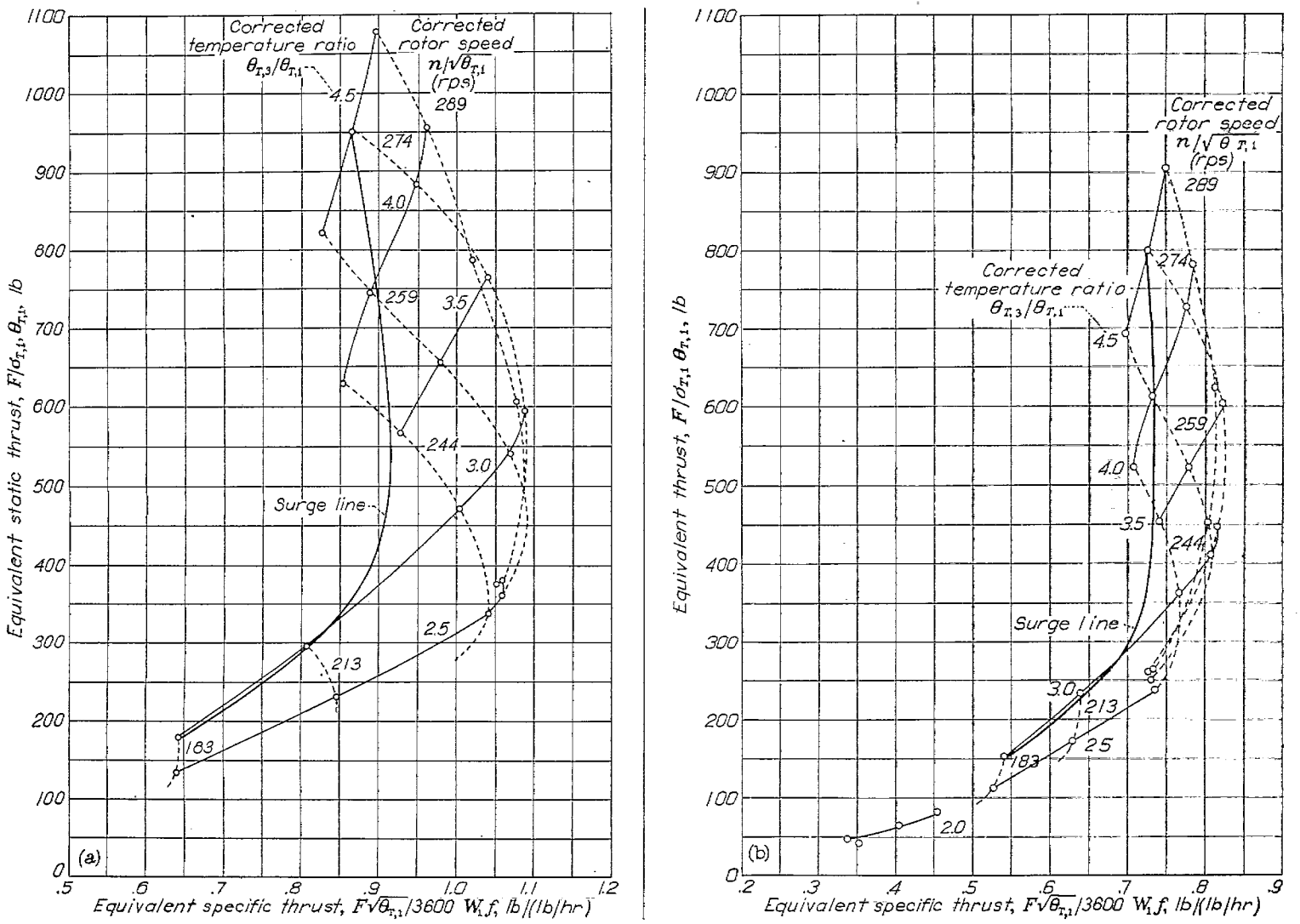

(a) Equivalent specific thrust: flight speed, 0 miles per hour; pressure altitude, 26,000 feet.

(b) Equivalent specific thrust: flight speed, 470 miles per hour; pressure altitude, 33,000 feet.

FIGURE 19.—Estimated characteristics of jet engine.

The minute effect of variations in γ during the nozzle-expansion process is neglected. The compressor characteristics give $\frac{W_1}{\sigma_{T,1}\sqrt{\theta_{T,1}}}$, and f is known for each point. The equivalent thrust is

$$\frac{F}{\sigma_{T,1}\theta_{T,1}}=\frac{1}{g}\left(\frac{W_1}{\sigma_{T,1}\sqrt{\theta_{T,1}}}\right)\left[(1+f)\left(\frac{c_5}{\sqrt{\theta_{T,1}}}\right)-\frac{V}{\sqrt{\theta_{T,1}}}\right] \quad \text{(lb)}$$

The equivalent power is

$$\frac{P}{\sigma_{T,1}(\theta_{T,1})^{3/2}}=\frac{1}{550}\left(\frac{V}{\sqrt{\theta_{T,1}}}\right)\left(\frac{F}{\sigma_{T,1}\theta_{T,1}}\right) \text{(hp)}$$

The specific thrust is

$$\left(\frac{F}{\sigma_{T,1}\theta_{T,1}}\right)\Big/\left[3600\left(\frac{W_1}{\sigma_{T,1}\sqrt{\theta_{T,1}}}\right)\left(\frac{f}{\theta_{T,1}}\right)\right] \text{(lb/(lb/hr))}$$

And the specific fuel consumption is

$$\frac{3600\left(\frac{f}{\theta_{T,1}}\right)\left(\frac{W_1}{\sigma_{T,1}\sqrt{\theta_{T,1}}}\right)}{\frac{P}{\sigma_{T,1}(\theta_{T,1})^{3/2}}} \text{(lb)/(hp-hr)}$$

From the weight flow and the outlet conditions, the area of the thrust nozzle can also be computed for each operating point and the correct nozzle selected for any desired condition.

The computed engine performance is shown for zero flight speed in figure 19 (a), which gives equivalent static thrust and equivalent specific thrust for constant values of corrected rotor speed and corrected temperature ratio. A similar chart is shown in figure 19 (b) for a flight speed of 470 miles per hour at an altitude corresponding to the same compressor-inlet pressure. At the same flight speed and altitude, figure 19 (c) shows the specific fuel consumption. The minimum estimated specific fuel consumption at 470 miles per hour is 0.885 pound per horsepower-hour at 550 pounds equivalent thrust, a temperature ratio of 3.35, a corrected compressor speed of 274 revolutions per second, and pressure ratio of 4.4.

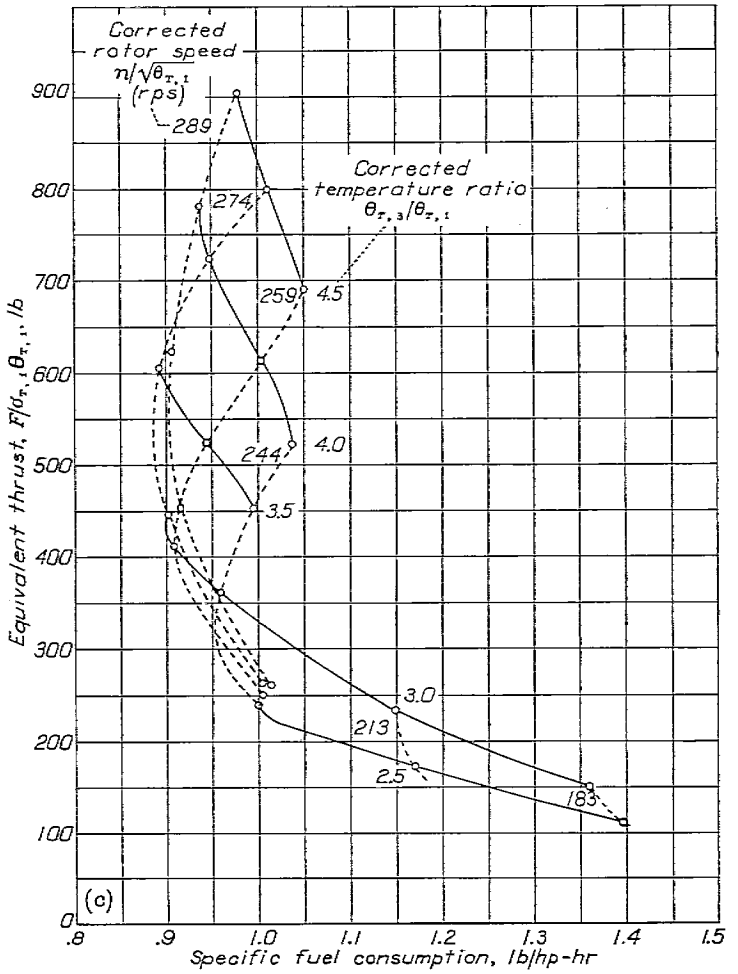

(c) Specific fuel consumption: flight speed, 470 miles per hour; pressure altitude, 33,000 feet.

FIGURE 19.—Concluded.

An estimate was made of the change in performance for an improvement in the matching of the turbine with the compressor. At the point where the static thrust was 788 pounds and the specific thrust 1.024 pounds per pound fuel per hour, the compressor speed was 289 revolutions per second, the corrected temperature ratio was 3.5, and the turbine efficiency, 0.82. The assumption was made that the changed turbine gave the peak efficiency of 0.875 at that corresponding point on the turbine matching chart. The thrust was increased to 826 pounds and the specific thrust to 1.073 pounds per pound fuel per hour, an improvement of 4.7 percent. The improvement at 470 miles per hour was about 4.7 percent in all performance parameters.

A study of the problem of engine adjustment for better matching is required in order to apply the knowledge gained from the matching charts. The manner in which the turbine and compressor performance characteristics must be altered in order to get an exact superposition of the maximum-efficiency regions of turbine and compressor with optimum engine performance must be determined.

OTHER APPLICATIONS OF MATCHING CHARTS

The matching charts described can be applied to engines other than the simple jet engine. Essentially the jet engine is a hot-gas producer, for which the matching charts will determine the state of the discharged gas. If this gas is discharged into a reheater and from there into a power turbine, the matching charts can be used to find the over-all performance for an engine of this type. In the general case of the turbine-propeller engine with jet power, a chart similar to the simple jet-engine chart may be used with a different vertical shift of the scales for each value of propeller torque.

Another type of generalization is possible by the use of different matching functions. For example, if the turbine is geared to the compressor, the gear ratio may be so incorporated into the functions that the turbine and compressor functions match. The engine with a single power turbine and no jet power may be studied by use of the isentropic-enthalpy-drop factor instead of the torque factor, which permits a matching of the pressure drop. In this case, a vertical logarithmic scale is advised because a simple shift in the vertical direction will give matching requirements with various ram-pressure ratios.

SUMMARY OF RESULTS

The following results were obtained from an investigation of the performance with cold air of the NACA two-stage turbine and the first stator-ring component:

1. The stream-filament method of checking turbine-blade pressure distribution gave blade velocity distributions that generated boundary layers of momentum thickness of about 0.0037 inch for the suction surface.

2. The energy loss in the wake of the blades engendered by the blade edge and the boundary-layer momentum thickness caused an estimated decrease in turbine efficiency of 0.2 percent. The increment in drag caused by boundary layer at the trailing edge is negligible.

3. The boundary layer at the shrouds built up to some extent inside the channel section of the nozzle but mainly downstream of the nozzle throat. This process was activated chiefly by the low pressure on the projecting surface of the blade.

4. The boundary layer on the stationary inner shroud was thick compared with that on the outer shroud, was stable, and built up with increasing air flow. The boundary layer on the outer shroud was thin, unstable, and decreased in thickness as the air flow was increased.

5. The boundary layer at the inner shroud blocked part of the flow area and established high axial velocities in the region adjacent to the inner boundary layer but downstream of the cascade. The boundary layer apparently had no other effect on the velocity distribution induced by the blades.

6. The effective annular area was about 0.875 of the actual area. At the design pressure ratio, the computed flow was 0.95 and the measured flow 0.964 of design. At design enthalpy drop, the flow was 0.98 of the design value. The difference between the flow reduction and the area reduction was probably caused by the build-up of the boundary layer of the inner shroud on the projecting suction surface of the blade without greatly affecting the flow in the nozzle throat.

7. At design value of the equivalent torque and the product of equivalent air flow and equivalent rotor speed ($W_3 n/\sigma_{T,3}\theta_{T,3}$, where W is gas flow, n is rotative speed, σ and θ are the density and temperature corrections, respectively, and T signifies total and 3 the turbine inlet), the efficiency was 0.823 as compared with the peak of 0.875 at a speed of 180 revolutions per second, which was the principal discrepancy between the design and measured results.

8. A set of charts was developed, which permits an estimate of jet-engine performance from the performance of the components and a determination of the degree of matching of the components.

9. The matching charts showed that the best compressor-efficiency region did not coincide with the best turbine-efficiency region when the two components were used as a jet engine. The peak compressor efficiency was 0.84 and the peak turbine efficiency 0.875. The peak compressor efficiency occurred at a corrected temperature ratio of 3.5 and a corrected rotor speed of 274 revolutions per second. At this point, the turbine operated at an efficiency of only 0.82. The point of minimum specific fuel consumption of the engine at 470 miles per hour and 33,000 feet is 0.885 pound per horsepower-hour with a corrected thrust of 550 pounds.

10. An estimate of the improvement in over-all engine performance was made for engine operation at a corrected temperature ratio of 3.5 and a corrected engine speed of 289 revolutions per second, under the assumption that the turbine could be adjusted to operate at its peak efficiency of 0.875 instead of the estimated operating efficiency of 0.820 for this engine condition. The improvement in engine performance was about 4.7 percent for all parameters at flight speeds of 0 and 470 miles per hour. This improvement might be regarded as available through improved matching of the two engine components.

CONCLUSIONS

This investigation indicated the probable general validity of the following conclusions:

1. The stream-filament method of checking turbine-blade pressure distribution proves satisfactory for obtaining high-solidity blades in a pressure-drop flow without thick boundary layers. Discharge guidance in the blades gives desired average moment of momentum, but incorrect angles near the blade roots.

2. The assumption of free-vortex flow and uniform axial velocity between blade rows is inadequate for estimating flow angles or weight-flow pressure-ratio relations but is satisfactory for estimating weight-flow work-output relations and is therefore satisfactory for estimating the operating point of the compressor. For accurate design, the area blocked by the boundary layer in the nozzles and the radial flow caused by the boundary-layer thickening downstream of the stators should be taken into account. Some method must be evolved for predicting these effects from design data. Thick boundary layers are not expected downstream of rotors.

FLIGHT PROPULSION RESEARCH LABORATORY,
NATIONAL ADVISORY COMMITTEE FOR AERONAUTICS,
CLEVELAND, OHIO, *June 6, 1947*.

APPENDIX A

SYMBOLS

The following symbols are used in this report:

A_e effective flow area downstream of first turbine stator row, sq ft
a sonic velocity of gas, ft/sec
a_{st} standard-air sonic velocity, 1116.3 ft/sec
c gas velocity, ft/sec
$\bar{c}_a$ mass-averaged axial-velocity component, ft/sec
c_p specific heat of gas at constant pressure, ft-lb/(slug)(°F)
F thrust of engine, lb
f fuel-air ratio
g standard gravitational acceleration, 32.174 ft/sec^2
H enthalpy, ft-lb/slug
H_b enthalpy of fuel entering combustion chamber, ft-lb/slug
ΔH stagnation enthalpy drop in turbine, ft-lb/slug
ΔH_c stagnation enthalpy rise in compressor, ft-lb/slug
ΔH_s isentropic drop in stagnation enthalpy through turbine, ft-lb/slug
h heating value of fuel, ft-lb/slug
n rotative speed of turbine, rps
P thrust horsepower of jet engine
P_A auxiliary-power consumption (bearings), ft-lb/sec
p gas pressure, lb/sq ft
R gas constant, ft-lb/(slug)(°R)
r distance from axis of annular channel, ft
S gas entropy, ft-lb/(slug)(°R)
s blade pitch, ft
T gas temperature, °R
t blade trailing-edge thickness plus momentum thickness of boundary layer, ft
$t_f = t/(s \cos \varphi_N)$
V flight speed, ft/sec
W total weight flow of gas, lb/sec
w weight flow of gas in annulus bounded by inner shroud of cascade ring and radius r, lb/sec
γ ratio of specific heats of gas
δ momentum thickness of boundary layer, in.
η combustion-chamber efficiency
$\theta = a^2/a_{st}^2$
μ absolute viscosity of gas, slug/ft-sec
ρ gas density, slug/cu ft
ρ_{st} standard-air density, 0.002378 slug/cu ft
σ ρ/ρ_{st}
φ angle between normal to cascade axis and flow direction of gas or discharge angle of stator blades, deg

Subscripts:

0 free-stream condition
1 compressor-inlet condition
2 compressor-outlet condition
3 turbine-inlet condition
4 turbine-outlet condition
5 propulsion-nozzle condition
a axial-velocity component
N condition in nozzle throat of blade cascade
r blade-root condition
st standard-air condition
T stagnation condition
t blade-tip condition
u tangential-velocity component

883026—50——28

APPENDIX B

TRAILING-EDGE MOMENTUM LOSS

A uniform parallel flow of gas with pressure p_N, temperature T_N, density ρ_N, and velocity c_N flows between an infinite set of straight vanes of thickness t, pitch (along cascade axis) s, and angle φ_N with respect to the normal to the cascade axis. The gas discharges into a space with no vanes and attains a final state of ρ, T, p with direction angle φ and velocity c of axial component c_a and tangential component c_u. The continuity equation is

$$\rho_N c_N \cos\varphi_N \left(s-\frac{t}{\cos\varphi_N}\right)=\rho c_a s$$

The fraction of flow area blocked is

$$t_f=\frac{t}{s\cos\varphi_N}$$

and the continuity equation is

$$\rho_N c_N \cos\varphi_N (1-t_f)=\rho c_a \tag{B1}$$

The momentum equation for components normal to the cascade axis is

$$p_N s-ps=\rho c_a s(c_a-c_N\cos\varphi_N)=\rho s c_a^2\left(1-\frac{\rho/\rho_N}{1-t_f}\right) \tag{B2}$$

Because the flow is isoenergetic

$$c_p T_N+\frac{c_N^2}{2}=c_p T+\frac{c^2}{2} \tag{B3}$$

The loss in available energy is measured by the heat-dissipation integral

$$\text{loss per slug of fluid}=\int_{S_N}^{S} T\,dS \tag{B4}$$

where S is the entropy. From thermodynamics

$$\int_{S_N}^{S} T\,dS=\int_{T_N}^{T} c_p\,dT-\int_{p_N}^{p}\frac{dp}{\rho}=c_p(T-T_N)-\int_{p_N}^{p}\frac{dp}{\rho} \tag{B5}$$

The momentum equation for components along the cascade reduces to

$$c_N\sin\varphi_N=c_u \tag{B6}$$

The integral $\int_{p_N}^{p}\frac{dp}{\rho}$ is approximated by

$$\int_{p_N}^{p}\frac{dp}{\rho}=\frac{1}{2}\left(\frac{1}{\rho}+\frac{1}{\rho_N}\right)(p-p_N) \tag{B7}$$

From equation (B2)

$$\int_{p_N}^{p}\frac{dp}{\rho}=\frac{p-p_N}{2\rho}\left(1+\frac{\rho}{\rho_N}\right)=\frac{c_a^2}{2}\left(\frac{\frac{\rho}{\rho_N}}{1-t_f}-1\right)\left(1+\frac{\rho}{\rho_N}\right)$$

Substitution of this relation as well as equations (B3) and (B6) into equation (B5) gives

$$\int T\,dS=\frac{c_{a,N}^2-c_a^2}{2}-\frac{c_a^2}{2}\left(\frac{\rho}{\rho_N}\frac{1}{1-t_f}-1\right)\left(1+\frac{\rho}{\rho_N}\right)$$

The quantity $c_{a,N}$ is eliminated by means of the continuity equation (B1)

$$\int T\,dS=\frac{\rho}{\rho_N}\frac{c_a^2}{2}\left(\frac{\frac{\rho}{\rho_N}}{1-t_f}-1\right)\left(\frac{t_f}{1-t_f}\right) \tag{B8}$$

From the equations of state, energy, and continuity

$$p-p_N=R(\rho T-\rho_N T_N)=RT(\rho-\rho_N)+R\rho_N(T-T_N)$$

$$=RT(\rho-\rho_N)+\frac{R\rho_N}{2c_p}(c_N^2\cos^2\varphi_N-c_a^2)$$

$$=RT(\rho-\rho_N)+R\rho_N\frac{c_a^2}{2c_p}\left[\left(\frac{\rho}{\rho_N}\right)^2\frac{1}{(1-t_f)^2}-1\right]$$

When this pressure difference is equated to that found from the momentum equation and ρ/ρ_N is eliminated by use of the variable $[(\rho/\rho_N)/(1-t_f)]-1$, a quadratic equation is obtained with the exact solution

$$\left(\frac{\rho}{\rho_N}\right)\left(\frac{1}{1-t_f}\right)-1=\frac{1-\gamma M_a^2(1-k)}{2\gamma M_a^2\left(1-\frac{k}{2}\right)}\left\{1-\sqrt{1-\frac{\frac{4t_f}{1-t_f}\gamma M_a^2\left(1-\frac{k}{2}\right)}{[1-\gamma M_a^2(1-k)]^2}}\right\}$$

where $M_a^2\equiv\frac{c_a^2}{\gamma RT}$ and $k\equiv\frac{\gamma-1}{\gamma(1-t_f)}$. For

$$\frac{4\frac{t_f}{1-t_f}M_a^2}{[1-\gamma M_a^2(1-k)]^2}<<1$$

the approximate solution is

$$\frac{\rho}{\rho_N}\frac{1}{(1-t_f)}-1\approx\frac{\left(\frac{t_f}{1-t_f}\right)}{1-\gamma M_a^2(1-k)} \tag{B9}$$

Equation (B9) is substituted in equation (B8) together with $\rho/\rho_N=1$ for the first factor to obtain the approximate answer

$$\int T\,dS\approx\frac{c_a^2}{2}\frac{\left(\frac{t_f}{1-t_f}\right)^2}{1-\gamma M_a^2(1-k)}(1-t_f)\left[1+\frac{\frac{t_f}{1-t_f}}{1-\gamma(1-k)M_a^2}\right]$$

$$\int T\,dS\approx\frac{c_a^2}{2}\frac{\left(\frac{t_f}{1-t_f}\right)^2}{1-\frac{c_a^2}{RT}\left[1-\frac{(\gamma-1)}{\gamma(1-t_f)}\right]} \tag{B10}$$

REFERENCES

1. Sinnette, John T., Jr., Schey, Oscar W., and King, J. Austin: Performance of NACA Eight-Stage Axial-Flow Compressor Designed on the Basis of Airfoil Theory. NACA Rep. No. 758, 1943.
2. Sinnette, John T., Jr., and Voss, William J.: Extension of Useful Operating Range of Axial-Flow Compressors by Use of Adjustable Stator Blades. NACA ACR No. E6E02, 1946.
3. King, J. Austin, and Regan, Owen W.: Performance of NACA Eight-Stage Axial-Flow Compressor at Simulated Altitudes. NACA ACR No. E4L21, 1944.
4. Stodola, A.: Steam and Gas Turbines. Vol. II. McGraw-Hill Book Co., Inc., 1927, pp. 992–994. (Reprinted, Peter Smith (New York), 1945.)